Assessment of the in-plane biomechanical properties of human skin using a finite element model updating approach combined with an optical full-field measurement on a new tensile device

Gaetan Boyer, Jérôme Molimard, Mohamed Ben Tkaya, Hassan Zahouani, Marc Pericoi, Stéphane Avril

Assessment of the in-plane biomechanical properties of human skin using a Finite Element Model Updating approach combined with an optical full-field measurement on a new tensile device

G. Boyer [a, b] - J. Molimard[c] [1]- M. Ben Tkaya[a, b] - H. Zahouani[a] - M. Pericoi[b] - S. Avril[c]

[a] Laboratory of Tribology and Systems Dynamics UMR5513 CNRS/ECL/ENISE/EMSE, 36 avenue Guy de Collongue, 69134 Ecully, France

hassan.zahouani@ec-lyon.fr

[b] Laboratoire PERITESCO,

18 Avenue de l'Opéra,

75001 Paris, France

gaetan.boyer@peritesco.com

mohamed.bentkaya@peritesco.com

marc.pericoi@peritesco.com

[c] LGF, UMR 5146, Ecole Nationale Supérieure des Mines, CIS-EMSE, CNRS,

Saint-Etienne, France

avril@emse.fr

molimard@emse.fr

1 Corresponding author, phone: 33 4 77 42 66 48

ABSTRACT.

Human skin is one of the most important organ of the body. The assessment and knowledge of its properties are very useful for clinical or cosmetic research. Many techniques are used to measure the mechanical properties of this organ, like suction, indentation, torsion or tension tests. The aim of this paper is to present a new device based on tension technique and combining mechanical and optical measurements. The whole procedure used to assess to the displacement field is described, and first results of tests performed *in vivo* are shown.

GRAPHICAL ABSTRACT.

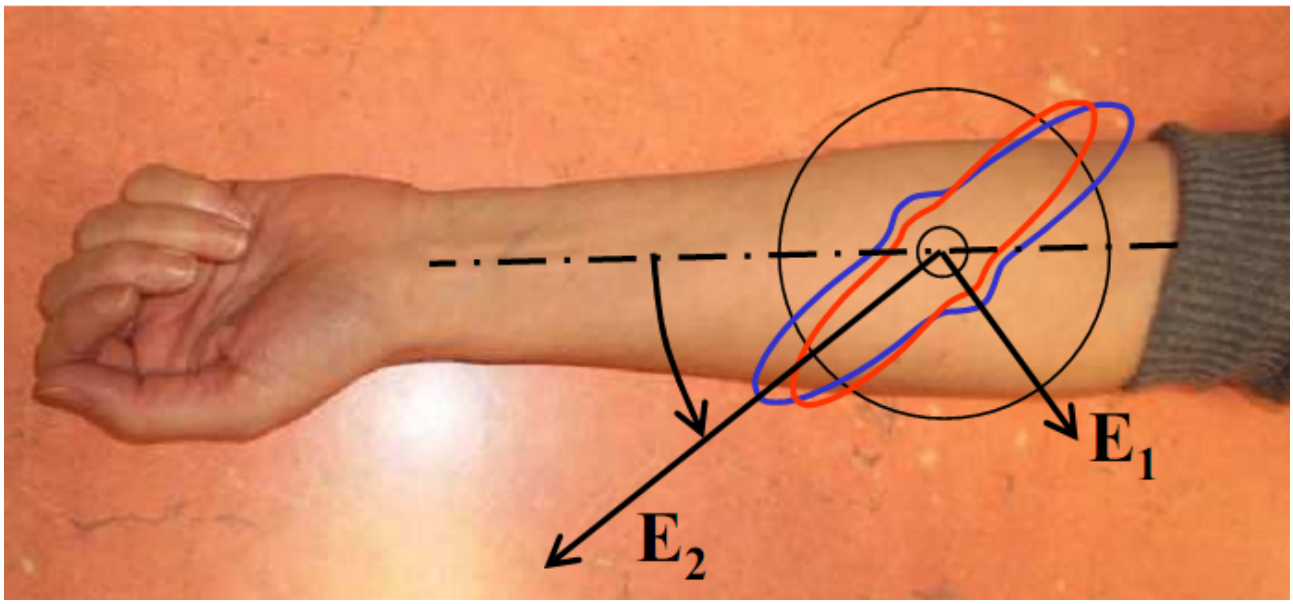

HIGHLIGHTS.

- A novel dedicated in plane traction / compression test device for in vivo skin analysis is presented
- Provided results are displacement maps and reaction forces results
- Skin properties are estimated by coupling the results to a Finite Element Model
- Anisotropy is quantified, and its evolution studied for young (blue) or old (red) age group.

KEY WORDS: extensometer, full field measurement, skin, mechanical properties.

1 Introduction

The skin is the heaviest and the vastest organ of the human body, and certainly one of the most important part. Its function of interface between the body and the external environment is vital. Skin must have very particular properties to permit exchange, for example perspiration, but also to protect the body against different types of attacks (mechanical, chemical or biological). The skin is composed of three main layers, the epidermis, the dermis and the hypodermis with different properties. At a mechanical point of view, skin is a very complex structure: it is an heterogeneous, visco-elastic, anisotropic, adhesive material showing a non linear stress-strain relationship (Agache et al., 2000). Moreover, the skin has a non zero natural tension. The measurement and the knowledge of these mechanical properties *in vivo* is essential for various domains, for example for clinical (assessment of the evolution of a pathology) or cosmetic (assessment of the efficiency of a product) research. Many different devices, using various techniques, have been developed to evaluate the mechanical state of the skin, like suction (Diridollou et al., 2000), contact (Jachowicz et al., 2007), (Pailler et al., 2008), (Boyer et al., 2009), or contactless indentation (Boyer et al., 2012), torsion (De Rigal, 2002) or extension (Thacker et al., 1977), (Vescovo et al., 2002), (Lim et al., 2008) tests. Extension test principle consists in attaching two pads on the skin and recording the forces induced by a tangential movement of one or both pads.

These previous studies showed that the skin is a visco-hyper-elastic and anisotropic material, with a complex initial tension. A lot of work have addressed in the past hyperelasticity (Manan et al., 2012) or viscosity (Boyer et al., 2009), but few work investigated the anisotropy. If considering the whole in-plane behaviour, with a simplification of the anisotropy to orthotropy, the number of variables should be 14 making very difficult a proper characterization. This paper aims at a specific characterization of anisotropy under the hypothesis of linear elastic orthotropy. This is made possible by using a small strain change, representative of skin strain variations during everyday life (10 %). Consequently results will be *apparent elastic moduli*. As the sought behaviour is anisotropic, the complete evaluation of its properties with this test considering only forces assessment requires several measurements with different directions. Last, in order to have the best contactless evaluation of strain and to improve the understanding of the skin behaviour, it can be very interesting to evaluate the strain field between the pads in addition to the forces during extension test (Marcellier et al., 2001).This paper presents a new device specially developed to this aim, the whole method used to assess the displacement field of the stressed area, and a complete analysis of the results using inverse approach (Finite Element Model Updating).

2 Methods

2.1 Device

The device is shown in figure 1. It is divided into two parts, the "mechanical" part, which aim is to move the pad and to measure forces and displacement, and the "optical" part, whose aim is to visualize and to record images of the deformed area. The whole acquisition chain is described in part 2.3.

{figure 1 should be placed here}

2.1.1 Mechanical part

The extensometer is composed of a static and a movable pad attached to the skin by double-sided adhesive. The choice of a static pad permits to measure the force due only to the stressed area. Indeed, the movable pad measures the force of the stressed area in addition to the force due to the surrounding area. The size of the pads can be 10×10, 20×20 or 20×50 mm^2. The gap between the pads ranges from 2 to 27 mm. Extension or compression tests can be performed. Each pad is mounted on a piece fixed onto a tangential force sensor, itself fixed onto a normal force sensor (all force sensors are load cells with full Wheatstone bridge). The normal force sensors allow to control the pressure applied by the pads on the skin. This point has been discussed by (Lim et al., 2008) and seems to be very important to improve the accuracy of the measurement. Ideally, tests are performed with a normal force oscillating around zero. Remaining oscillations are related to the patient movements (breathing, hearth beat) . The full scale of normal sensors is 3N and the full scale of tangential sensors is 10N. The normal sensor of the static pad is bonded onto the frame, and the normal sensor of the movable pad is bonded onto the movable part of a micrometric motorised translation stage (Polytech Instrument) controlled by computer. This translation stage allows a movement with a velocity ranging from 0.1 to 1.5 mm/s with an accuracy less than 1 µm. The static part of this translation stage is bonded onto the frame. The frame is mounted on a manual translation stage, which permits to control the normal pressure applied by the pads. This manual translation stage is itself mounted on a complete movable frame allowing X,Y,Z movement and rotation using a ball pivot. This frame and a picture of *in vivo* measurement on the arm are shown in figure 2.

{Figure 2 should be placed here}

2.1.2 Acquisition chain

Signals of the force sensors are converted into voltage using two bridge conditioners PMI-301B (PM Instrumentation) and recorded using a 16 bits acquisition card NI 6221-M (National Instrument). Images are recorded through USB-2 port. The translation stage is controlled by a

supplier card PI C-843 (Polytech Instrument). In order to have the best synchronisation possible between forces and displacement signals, the position of the stage is directly recorded using internal counter of the acquisition card. A program developed under LabView environment drives the whole system.

2.1.3 Optical part

The image acquisition of the stressed area is performed by an 8 bits camera (The Imaging Source) placed over the pads with high quality optics (deformation less than 0.1%). A micro metric manual translation stage allows to set up the focal length. The field of view is 1280×960 pixels^2, corresponding to an area of 20×15 mm^2 (15.6 µm/pixel). During the test, images are recorded at a frequency of 10 frames/s. The lighting of the area is very important. It is performed by two groups of three blue (λ= 470 nm) LEDS in order to minimize the diffusion of the light into the skin. Indeed, the lower the wavelength of the light, the less the penetration. LEDS technology gives an illumination with a negligible heating compared with other technologies. Last, the bulk volume size is very low, leading to a very compact system. A laser projects a line on the stressed area in order to measure a profile. This function is not described in this paper.

2.2 Full field measurement method

An example of an image recorded by the camera is shown figure 3. It is used to find the displacement field between the first and the last image of the test. The method used is based on Digital Image Correlation (DIC) (Sutton et al., 2009), and has been presented extensively in (Molimard et al., 2010). So far, only the basic principle is given here.

{figure 3 should be placed here}

2.2.1 2D Digital image correlation

Assuming a reference image im0 described by $f(r,s)$, a deformed image im1 of im0 after a small deformation is described by $g(r,s)$ by the following equation:

$$g(r,s) = f(r-\delta_x, s-\delta_y) + b(r,s) \tag{1}$$

where δx and δy are the components of the displacement of im1 and $b(r,s)$ the noise measurement. A way to find δx ans δy is to maximize function h defined by:

$$h(r,s) = (g * f)(r,s) = \int_{-\infty}^{+\infty}\int_{-\infty}^{+\infty} g(a,b) f(a-r, b-s)\, da\, db \tag{2}$$

where * denotes the cross-correlation product. Found values of r and s found correspond to the maximal probability of displacement (δx, δy). This method can be applied in Fourier space using Fast Fourier Transform function, noted FFT2D. Equation 1 becomes:

$$g * h = FFT2D^{-1}\left(FFT2D(g)\,\overline{FFT2D(f)}\right) \tag{3}$$

where the over-line denotes the complex conjugate. Equation 1 and 3 are used at a local scale, on a typical 32×32 zone of interest (ZOI). The procedure is repeated all over the map, giving a final displacement field.

Now, classical digital image correlation performs the cross-product either in Fourier or real space. More refined approaches exist by the way: for example, the signal could be normalized with respect to the mean local intensity, and/or the mean local contrast (Bornert, 2009). The cross-correlation peak is commonly interpolated in order to reach a sub-pixel displacement accuracy. The interpolation function can be a Gaussian or polynomial function. Basically, this choice does not have a strong theoretical basis, and authors generally have an empirical approach. We propose hereafter an alternative to this weak point in the image correlation approach.

2.2.2 Sub-Pixel algorithm

The sub-pixel algorithm is based on the local analysis of ZOI. The random intensity pattern can be described as a sum of periodic functions using a classical Fourier expansion. Then, the random intensity pattern (the speckle signature) can be decomposed into a sum of period patterns (fringes); finally, this approach is a generalization of the grid method, well adapted to small displacement estimation. Because Fourier Transform requires continuity, the ZOI is windowed using a bi-triangular function. So far, the algorithm is an extension of the Windowed Fourier Transform (WFT) algorithm proposed by Surrel (Surrel, 1996). As shown Fig. 4, in the frequency domain, each couple of frequencies is characterized by an amplitude and a phase. This phase is proportional to the displacement normal to the corresponding fringe direction. Note that the phase is defined only if the amplitude is higher than zero. Then, in absence of any phase jump, displacements can be related to any defined phase using the relationship:

$$\begin{Bmatrix} \vdots \\ \Delta\varphi_\theta^i \\ \vdots \end{Bmatrix} = \underbrace{\begin{bmatrix} \vdots & \vdots \\ \frac{2\pi}{p_\theta^i}\cos\theta^i & \frac{2\pi}{p_\theta^i}\sin\theta^i \\ \vdots & \vdots \end{bmatrix}}_{A} \begin{Bmatrix} \delta_x \\ \delta_y \end{Bmatrix} \tag{4}$$

where $\begin{Bmatrix} \vdots \\ \Delta\varphi_\theta^i \\ \vdots \end{Bmatrix}$ is a vector containing all the phase differences, $\begin{Bmatrix} \delta_x \\ \delta_y \end{Bmatrix}$ is the displacement vector, and A is the sensitivity matrix. A is a rectangular matrix with 2 rows and as many lines as defined

phases, up to 255 in usual conditions.

Displacements can then be derived from eq. 2 using the pseudo-inverse of A. This operation is possible if $\det\left(\left(A^t A\right)\right) \neq 0$. In practice, this means that at least two phases along two different directions exist.

$$\begin{pmatrix} \delta_x \\ \delta_y \end{pmatrix} = \left(A^t A\right)^{-1} A^t \begin{pmatrix} \vdots \\ \Delta\phi_\theta^i \\ \vdots \end{pmatrix} \tag{5}$$

Practical problem of this approach is that the signal to noise ratio is weak for each couple of frequencies. Then, the quality of the measurement is obtained by averaging all the available information throw the pseudo-inverse function. A detection of erroneous phases is implemented in order to increase the system resolution.

One should note also that a phase jump can occur in the Fourier domain. Even if a specific treatment should be developed, it sounds better to use first a pixel correlation algorithm. This ensures that the two ZOIs will be as superimposed as possible and that the fringe order is zero for any point and any couple of frequencies. No deformation of the ZOI is proposed here, considering that target applications will be in the small transformation domain.

{figure 4 should be placed here}

2.2.3 Application to the skin

The information used for DIC on human skin is contained in the surface texture. Therefore, the ZOI has to be adjusted to the skin signature [Bornert et al., 2009, Badulescu et al., 2013]. Considering the global framework of the Nyquist–Shannon sampling theorem, ZOI size should be strictly higher than 2 times the speckle size. Here, ZOI size has been set to 32, which corresponds to a spatial resolution of 8 pixels i.e. 125 µm (80 % radius of the autocorrelation function). Indeed, it isn't our purpose to detect movements at the wrinkle scale but at a more global level. So far, the phenomenon is low-frequency, so a minimization of the spatial resolution is not critical. A repeatability test showed a resolution of 0.03 px, i.e. 0.5 µm.

During the test, the texture changes, with appearance of new furrows in the direction of the stress, and disappearance of furrows perpendicular to this direction, as shown in figure 5.

{Figure 5 should be placed here}

In this case, DIC cannot be performed, because information in the reference and deformed images are too different. The way to solve this problem is to perform correlation between successive images recorded throughout the test. If *N* is the number of images, we obtain then *N-1* displacement maps. The problem is to reconstruct the complete displacement fields with the first image as the reference. We use the finite element method as described by (Avril et al., 2008a). The principle of the method is to mesh the area of interest for each map and to search the reconstructed fields U_{recx} and U_{recy} which minimize an error function *F* between values at the nodes of the mesh and the experimental data. The reconstructed displacement fields can then be interpolated between each node of the mesh and summed to obtain the displacement fields between the first and the final image.

2.3 Identification of mechanical parameters

2.3.1 Modelling skin mechanical behaviour

Results obtained through the experimental set-up are forces and displacement fields: information potentially lead to mechanical properties of the skin, if an appropriate identification strategy is developed. As a matter of fact, because the stress cannot be deduced from simple assumptions, the mechanical test is not a simple one, and an inverse procedure has to be adopted. In the recent years, identification from optical full field technique has been widely used for inert materials, following different kind of behaviour law, for example anisotropic elasticity (Grediac et al., 1998), damage propagation (Claire et al., 2004) or plasticity (Avril et al., 2008b). Methods could be adapted for each case. In the present study, we followed first works using Finite Element Model Updating (Molimard et al., 2005), later developed and optimized by Silva (Silva et al., 2007) because of its versatility.

Here, two main problems have to be addressed: the skin behaviour law and the mechanical model. Skin behaviour law should be described as a visco-elastic, anisotropic, non linear model and/or with pre-tension (Hendricks, 2001). In this work, if noting that test speed should only exhibit elasticity without viscous effects, and considering that the applied load is small enough not to change the instantaneous stiffness, the behaviour law could be linear elastic. It is proposed here to use an orthotropic linear elastic model for the identification procedure. The resulting value can be seen as a secant definition of the elastic parameters, even if the real elastic behaviour corresponds to a more general law. Note that the skin layers are not represented in this description: the chosen test is

purely in-plane, thus is not sensitive to changes across the skin thickness, as found using the Classical Laminate Theory (Tsai, 1980).

2.3.2 Finite Element Model

In the FE model, the skin is idealized as a plate (figure 6). Pads are represented by two areas with a controlled displacement, one being zero, the other corresponding to the displacement in the experiment. This implies that we assume zero sliding under the pads; this assumption could be controlled with the image correlation system.

The plate is clamped on its boundaries in order to take into account the load transmission around the static pad. Consequently, the problem is to find the right dimensions around the area of interest (between the pads). Here, the idealized skin is supposed to be a square in order to minimize the number of unknown variables. Then the size of the square is tuned in such a way that the force ratio between the movable and the static pad were as close as possible to the experiment. Using a 100 mm square plate, 1mm thick, a material behaviour corresponding to commonly accepted values for skin (E_1 = 1 MPa, E_2 = 0.5 MPa, G_{12} = 0.4 MPa, ν_{12} = 0.4) and the angle between the orthotropic frame of reference and the forearm axis $\alpha = 20°$, the obtained ratio is close to 2.02 when the mean experimental value is 2.08, minimum and maximum values being respectively 1.7 and 2.7 (see “Results” section).

Last, the plate is meshed using quadratic elements outside the zone of interest, and triangular elements inside the zone of interest. This choice is made to optimize the number of elements (and the calculation time) but also to have the same interpolation procedure and meshing elements both in the experimental and in the numerical procedure. Mean element size within the zone of interest is 0.67 mm.

{Figure 6 should be placed here}

2.3.3 Identification procedure

The numerical model should be controlled either on displacement or force. If it were controlled on the displacement the cost function would have involved a distance between the calculated force and the experimental force in the cost function, the two distance terms (on displacement and on force) balanced using a penalty parameter. First tests using such a cost function showed the importance of the penalty term, and the great difficulties in tuning this parameter. Consequently, this approach has been discarded, and the control on force is directly ensured by the finite element code.

The cost function is established for *N* experimental points for each of the for *m* load cases used in this study:

$$F = \frac{1}{2}\sum_{j=1}^{m}\left(\sum_{i=1}^{N}\left(\frac{u_{(i,j)}^{exp}-u_{(i,j)}^{num}}{max\left(u_{(i,j)}^{exp}\right)-min\left(u_{(i,j)}^{exp}\right)}\right)^2+\left(\frac{v_{(i,j)}^{exp}-v_{(i,j)}^{num}}{max\left(v_{(i,j)}^{exp}\right)-min\left(v_{(i,j)}^{exp}\right)}\right)^2\right) \quad (6)$$

where (u^{exp}, v^{exp}) refers to the experimental displacements, and (u^{num}, v^{num}) refers to the numerical displacements.

The optimization algorithm used here is a boundary Levenberg Marquardt method, developed by Le Riche (Guyon et al., 2000). This gradient method uses the Hessian matrix H, the identification parameters being denoted $x_1, \ldots x_n$.

$$H(F) = \begin{bmatrix} \frac{\partial^2 F}{\partial x_1^2} & \frac{\partial^2 F}{\partial x_1 \partial x_2} & \cdots & \frac{\partial^2 F}{\partial x_1 \partial x_n} \\ \frac{\partial^2 F}{\partial x_2 \partial x_1} & \frac{\partial^2 F}{\partial x_2^2} & \cdots & \frac{\partial^2 F}{\partial x_2 \partial x_n} \\ \vdots & \vdots & \ddots & \vdots \\ \frac{\partial^2 F}{\partial x_n \partial x_1} & \frac{\partial^2 F}{\partial x_n \partial x_2} & \cdots & \frac{\partial^2 F}{\partial x_n^2} \end{bmatrix} \quad (7)$$

The study of this Hessian matrix gives information on the identifiability of the different parameters. We chose here to identify the compliance matrix, following previous study by Silva (Silva, 2009), but results will be given using engineering constants (E_1, E_2, G_{12}, ν_{12}) and the angle α for the sake of simplicity. This study clearly shows that the test developed here is insufficient to identify all the target parameters. Table 1 present an indicator of identifiability (ratio of the highest eigenvalue by the lowest eigenvalue of the Hessian matrix) for 4 different cases (traction along 0° direction, 0° and 90°; 0°, 45° and 90°; 0°, 45°, 90° and 135°).

{Table 1 should be placed here}

Finally, the starting point influence has been checked. Again, the number of test-cases is important: it is necessary to use at least 3 test-cases to achieve a successful identification for any starting point. This results shows that it is necessary to use a rich enough test to identify multiple parameters. Because of the poorness of the test used here, it is necessary to multiply the test conditions. In the following, 4 directions will be used.

3 Results

3.1 Validation

3.1.1 Force and displacement validation

Different tests have been performed to validate the device and the method. Calibration on force sensors has been performed on the whole device. We found sensitivity of 2.988 ±0.0012 and 2.830 ±0.0013 N/V for the static and movable normal sensors, and 0.492 ±0.0014 and 0.484 ±0.0016 N/V for the static and movable tangential sensors (evaluated with 5 loads). No hysteresis and no drift of these sensitivities have been observed.

Tests using a laser velocimeter have shown a minimal reproducible displacement of 1 µm, and a difference between the theoretical maximal speed is less than 5 % (normal load being 2 N).

3.1.2 Full field measurement method validation

Uncertainty sources are displacement errors due to noise propagation from the camera, algorithm accuracy, camera calibration i.e. pixel size and out-of-plane displacement. Noise propagation and algorithm accuracy have been evaluated through tests on simulated images of the skin with rigid body motion, simulated images of speckle with sine displacement of amplitude 0.2 and 0.02 pixels (Bornert et al., 2009), and skin images which simulate an extension with a static part at the bottom of the image. The resolution found was 0.03 pixels. Camera calibration is performed with the procedure proposed by (Bouquet, 2000). Last, out-of plane displacement is measured using the laser line. Expected vertical accuracy is 10 µm. Resulting uncertainty on the in-plane displacement field is 0.05 %. Finally, the overall error estimation without out-of-plane displacement has been evaluated as 0.12 % of the measured displacement.

Last, especially for *in vivo* tests, movements of the subject can also disturb the measurement. One should note also that surface optical signature changes when tension is applied. This point has been discussed previously in “Methods” section.

3.2 Experimental results

The *in vivo* test have been performed on the forearm of 2 groups of healthy young and old women, respectively 23.2 +/- 1.6 (10 subjects) and 60.4 +/6 2.4 (group 2, 10 subjects). Only one typical result is presented here for the seek of clarity (26 years old woman). The size of the pads was 10×10 mm^2, the initial gap was 10 mm, the displacement of the movable pad was an extension of 1 mm

with a velocity of 1 mm/s. The reference axis $\vec{U}$ is the axis of the forearm, and the angle between $\vec{U}$ and the axis of the tension test $\vec{Y}$ is noted α. 10 images were recorded during the test. Parameters used for the correlation were a size of subset images of 32×32 pixels^2 and a pitch of 4 pixels. In order to have coherent results, the mesh used for the first displacement reconstruction has been used for the others. Displacement fields and maximum load on static and movable pads for each direction are shown in figure 7 and figure 8 using 5% strain (0.5 mm of displacement on movable pad). Furthermore, we can also observe a difference of 41.6 %, 101.8 % and 86.3 % between the forces on static and movable pads respectively for 0°, 45°, 90° and 135° direction which confirm the influence of the surrounding area for the force measurement.

{Figure 7 should be placed here}

{Figure 8 should be placed here}

3.3 Identification results

Identification has been performed for each test-case, then results have been summarized as a mean value and a variation (at 95 % probability level). Anisotropy has been clearly outlined in Table 2, even if the variability is high: E_2 is 3.7 times higher than E_1. On the other hand, even if differences exist between the two groups, these differences are not significant using ANOVA procedure.

{Table 2 should be placed here}

Now, it is possible to draw the apparent stiffness according to the direction using Classical Laminate Theory (Tsai, 1980). The result is shown figure 9.

{figure 9 should be placed here}

4 Discussion

Displacement fields are very different depending of the stress direction (figure 7), and usually asymmetric, showing qualitatively a global anisotropy. The punctual force measurement results confirm the anisotropic behaviour of the skin (figure 8). Differences can be observed also between the two groups (young or old), with a higher anisotropy for young people, but also a difference in

the orientation of force frames. Only 8 on 32 test-cases are significantly different using ANOVA procedure. Indeed, the differences are too low compared to the variability among the groups. Finally, only the identification procedure gave quantitative estimate of the stiffness variations with the direction (Table 2).

The anisotropic behaviour has been taken into account using a simple orthotropic model at low strain. The results obtained expressed in term of Young's modulus can be linked to the whole behaviour observed with ageing. Indeed at low strain level the response of the tissue is mainly due to the elastin fibres network which is responsible to the natural tension state of the skin. This tension decreases with ageing. Then, the decrease of E1 and E2 for elder group should indicates a decrease in the pre-tension in both directions with the age: the higher the pre-tension is, the stiffer is the skin. This explanation is in good agreement with previous studies performed with other methods (Boyer et al., 2012). Note that this conclusion is valid only at low strain for which the response is mainly due to elastin network, higher strain inducing non linear behaviour with collagen fibres response.

Based on this observation, one should imagine as a future work, that the anisotropy can be modelled with a non uniform pre-tension field associated with elastic non linear law instead of an orthotropic behaviour model.

Last, the orientation of the stiffer axis with the arm has to be studied in the future. As a matter of fact, the relative angular position of the hand and the elbow is very important in the definition of a reference mechanical state of the skin. Here, the use of a complete positioning system ensures that the position is the same for all the patients (Figure 10), but one should note that forearm is twisted compared to the position at rest. The stiffer axis would probably be aligned with the forearm axis in the rest position.

Compared to previous studies (Khatyr et al., 2004), the richness of displacement fields makes possible a more realistic mechanical description, in particular by taking into account the skin reaction around the pad. Finally, the approach permits a full identification of all the parameters of the chosen orthotropic behaviour, including in particular the Poisson ratio value.

{Figure 10 should be placed here}

5 Conclusion

Measuring anisotropy of skin is a key feature to understand the injury recovery and scare formation. A complete device and method for the *in vivo* assessment of the displacement fields in addition to the forces during tension test has been presented. Results have been obtained on the forearm with 4 different traction orientations and with two groups of patients, selected according to their age; they clearly show the anisotropy of the skin by analysing 1/ the displacement fields 2/ the forces and reaction forces.

In a second step, this anisotropy has been evaluated using a complete identification procedure based on the Finite Element Updating Method. Given results are apparent elastic moduli, obtained for a 10% variation above the initial natural skin tension. Major stiffness is found to be 3.7 higher than the minor stiffness. The stiffer direction is mainly across the forearm, but this orientation would have be studied better in the future because of the major influence of the arm position. Even if the data are too scattered to give a clear trend, the stiffness is higher for the group of young patients than for the elder one. It has been proposed to explain this phenomenon with the variation of pre-tension in the skin with the age, in conjunction with the hyper-elastic behaviour of the skin. This assumption will be checked in the near future.

6 bibliography

[Agache et al., 2000] Agache, P.G., 2000. Physiologie de la peau et explorations fonctionnelles cutanées. Editions Medicales Internationales, ISBN: 2-7430-0360-X.

[Avril et al., 2008a] Avril, S., Feissel, P., Pierron, F., Villon, P., 2008. Estimation of the strain field from full-field displacement noisy data. Comparing finite elements global least squares and polynomial diffuse approximation. European Journal of Computational Mechanics, 17 (5-7), 857-868.

[Avril et al., 2008b] Avril, S., Pierron, F., Yan, J., Sutton, M.A., 2008. Identification of viscoplastic parameters and characterization of Lüders behavior using Digital Image Correlation and the Virtual Fields Method. Mechanics of Materials. 40 (9), 729-742.

[Badulescu et al., 2013] Badulescu C., Bornert M., Dupré J.-C., Equis S., Grédiac M., Molimard J., Picart P., Rotinat R., Valle, V., 2013. Demodulation of Spatial Carrier Images: Performance Analysis of Several Algorithms Using a Single Image, Experimental Mechanics, DOI 10.1007/s11340-013-9741-6.

[Bouquet, 2000] Bouguet, J.Y., 2008. Camera Calibration Toolbox for Matlab. *http://www.vision.caltech.edu/bouguetj/calib_doc/*

[Boyer et al., 2009] Boyer, G., Laquièze, L., Le Bot, A., Laquièze, S., Zahouani, H., 2009. Dynamic indentation on human skin in vivo: ageing effects. Skin Research and Technology, 15(1), 55-67.

[Boyer et al., 2012] G., Boyer, C., Pailler Mattei, J., Molimard, M., Pericoi, S. Laquieze, H. Zahouani, 2012. Non contact method for in vivo assessment of skin mechanical properties for assessing effect of ageing. Medical Engineering & Physics, 34, 172–178.

[Bornert et al., 2009] Bornert, M., Brémand, F., Doumalin, P., Dupré, J.C., Fazzini, M., Grédiac, M., Hild, F., Mistou, S., Molimard, J., Orteu, J.J., Robert, L., Surrel, Y., Vacher, P., Wattrisse, B., 2009. Assessment of Digital Image Correlation Measurement Errors: Methodology and Results. Experimental Mechanics, 49, 353–370.

[Claire et al., 2004] Claire, D., Hild, F., Roux, S., 2004. A finite element formulation to identify damage fields: the equilibrium gap method. International Journal for Numerical Methods in Engineering, 61 (2), 189-208.

[De Rigal, 2002] De Rigal, J., 2002. Hardware and basic principles of the Dermal Torque Meter..

Bioengineering of the skin - skin biomechanics. CRC Press, USA, New York, p. 63-76.

[Diridollou et al., 2000] Diridollou, S., Patat, F., Gens, F., Vaillant, L., Black, D., Lagarde, J. M., Gall, Y., Berson, M., 2000. In vivo model of the mechanical properties of the human skin under suction. Skin Research and Technology, 6(4), 214-221.

[Grediac et al., 1998] Grédiac, M., Pierron, F. 1998. A T-shaped specimen for the direct characterization of orthotropic materials. International Journal for Numerical Methods in Engineering, 41, 293-309.

[Guyon et al., 2000] Guyon, F., Le Riche, R., 2000. Least squares parameter estimation and the Levenberg-Marquardt algorithm: Deterministic analysis, sensitivities and numerical experiments, Technical Report INSA de Rouen, No. 041/99.

[Hendricks, 2001] Hendriks, F.M., 2001. Mechanical behaviour of human skin in vivo – a litterature review, Nat. Lab. Unclassified report 820, Philips research laboratories, 52 p.

[Jachowicz et al., 2007] Jachowicz, J., McMullen, R., Prettypaul, D., 2007. Indentometric analysis of in vivo skin and comparison with artificial skin models. Skin Research and Technology, 13 (3), 299-309.

[Khatyr et al., 2004] Khatyr, F., Imberdis, C., Vescovo, P., Varchon, D., Lagarde, J.M., 2004. Model of the viscoelastic behaviour of skin in vivo and study of anisotropy. Skin Research and Technology, 10(2), 96–103.

[Lim et al., 2008] Lim, K. H.,Chew, C. M., Chen, P. C. Y., Jeyapalina, S., Ho, H. N., Rappel, J. K., Lim B. H., 2008. New extensometer to measure in vivo uniaxial mechanical properties of human skin. Journal of Biomechanics, 41(5), 931-936.

[Marcellier et al., 2001] Marcellier H., Vescovo P., Varchon D., Vacher P., Humbert P., 2001. Optical analysis of displacement and strain fields on human skin. Skin Research and Technology, 7, 246–253.

[Manan et al., 2012] Manan N.F.A., Ramli M.H.M., Patar M.N.A.A.,Holt C., Evans S., Chizari M., Mahmud, J., 2012. Determining hyperelastic parameters of human skin using 2D finite element modelling and simulation. IEEE Symposium on Humanities, Science and Engineering Research (SHUSER), Kuala Lumpur, June 24-27. pp. 805-809.

[Molimard et al., 2005] Molimard, J., Le Riche, R., Vautrin, A., Lee, J.R., 2005. Identification of the four orthotropic plate stiffnesses using a single open hole tensile test, Experimental

Mechanics, Vol. 45 (5), 404-411.

[Molimard et al., 2010] Molimard, J., Boyer, G., Zahouani, H., 2010. Frequency-based image analysis of random patterns: an alternative way to classical stereocorrelation. Journal of the Korean Society of Non Destructive Testing, 30, 181-193.

[Pailler et al., 2008] Pailler-Mattei, C., Bec, S., Zahouani, H., 2008. In vivo measurements of the elastic mechanical properties of human skin by indentation tests. Medical engineering and physics, 30(5), 599-606.

[Silva et al., 2007] Silva, G., Le Riche, R., Molimard, J., Vautrin, A., Galerne, C., 2007. Identification of Material Properties using FEMU: Application to the Open Hole Tensile Test Applied Mechanics and Materials, 7-8, 73-78.

[Silva, 2009] Silva, G., 2009. Identification of material properties using finite elements and full-field measurements, PhD thesis, Ecole des Mines de Saint-Etienne, 226 pages.

[Surrel, 1996] Surrel Y., 1996. Design of algorithms for phase measurements by the use of phase stepping, Applied Optics, 35, 1, 51–60.

[Sutton et al., 2009] Sutton, M.A., Orteu, J., Schreier, H., 2009. Image Correlation for Shape, Motion and Deformation Measurements: Basic Concepts, Theory and Applications, Springer, 364 p., ISBN-10: 0387787461.

[Thacker et al., 1977] Thacker, J.G., Iachetta, F.A., Allaire, P.E., 1977. In vivo extensometer for measurement of the biomechanical properties of human skin. The Review of Scientific Instruments, 48(2), 181-5.

[Tsai, 1980] Tsai, S.W., Hahn, H.T., 1980. Introduction to composite materials, Technomic Pub., Lancaster, Basel, 457 pages.

[Vescovo et al., 2002] Vescovo, P., Varchon, D., Humbert, P., 2002. In vivo tensile tests on human skin: the extensometers. Bioengineering of the skin - Skin biomechanics. CRC Press, USA, New York, 77-90.

7 Table and Figures

Table 1. Identifiability of the 5 parameters for different test-cases, from 1 loading direction to 4 loading directions. Identifiability coefficient corresponds to the capacity to separate the effects from each material parameter.

Table 2. Identified results for young and old groups

~

Figure 1. Two views of the dDeveloped device.

Figure 2. Whole system withmounted on a movable frame (left). Measuring head can be rotated to fit with human body necessities, as shown on the right and (in vivo test on the arm (right).

Figure 3. View of the camera: static (a) and movable (b) pads, current frame of reference (x,y). Histogram (full scale: 256 grey levels) and Zone Of Interest (ZOI) have been represented on the upper and lower left angles.

Figure 4. Basic principle of sub-pixel algorithm.

Figure 5. Reference (left) and deformed (right) image of the same area.

Figure 6. Numerical model.

Figure 7. Displacement fields along and with various tension direction on a woman forearm (young group).

Figure 8. Tangential force F (in N) on static and movable pad (mean values for each group).

Figure 9. Apparent skin stiffness on the forearm according to the direction.

Figure 10. Forearm positioning apparatus.

1 test	2 tests	3 tests	4 tests
258.8	37.49	29.47	37.06

Table 1. Identifiability of the 5 parameters for different test-cases, from 1 loading direction to 4 loading directions. Identifiability coefficient corresponds to the capacity to separate the effects from each material parameter.

Group	E_1 (kPa)	E_2 (kPa)	G_{12} (kPa)	ν_{12}	α (°)
Young	40±7	146±69	14±4	0.062±0.061	37.57±6.52
Old	29±10	130±68	12±5	0.109±0.045	44.94±9.35

Table 2. Identified results for young and old groups

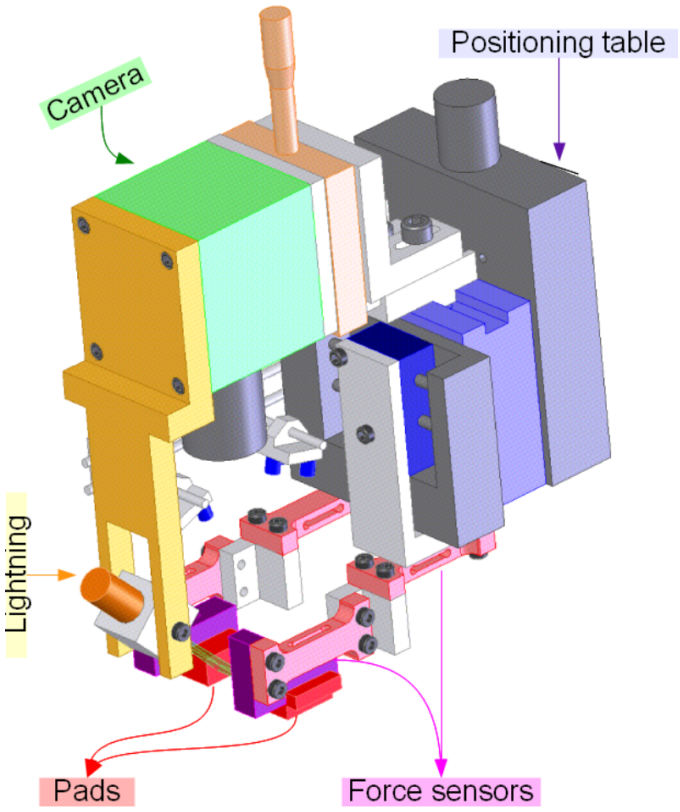

Figure 1. Developed device.

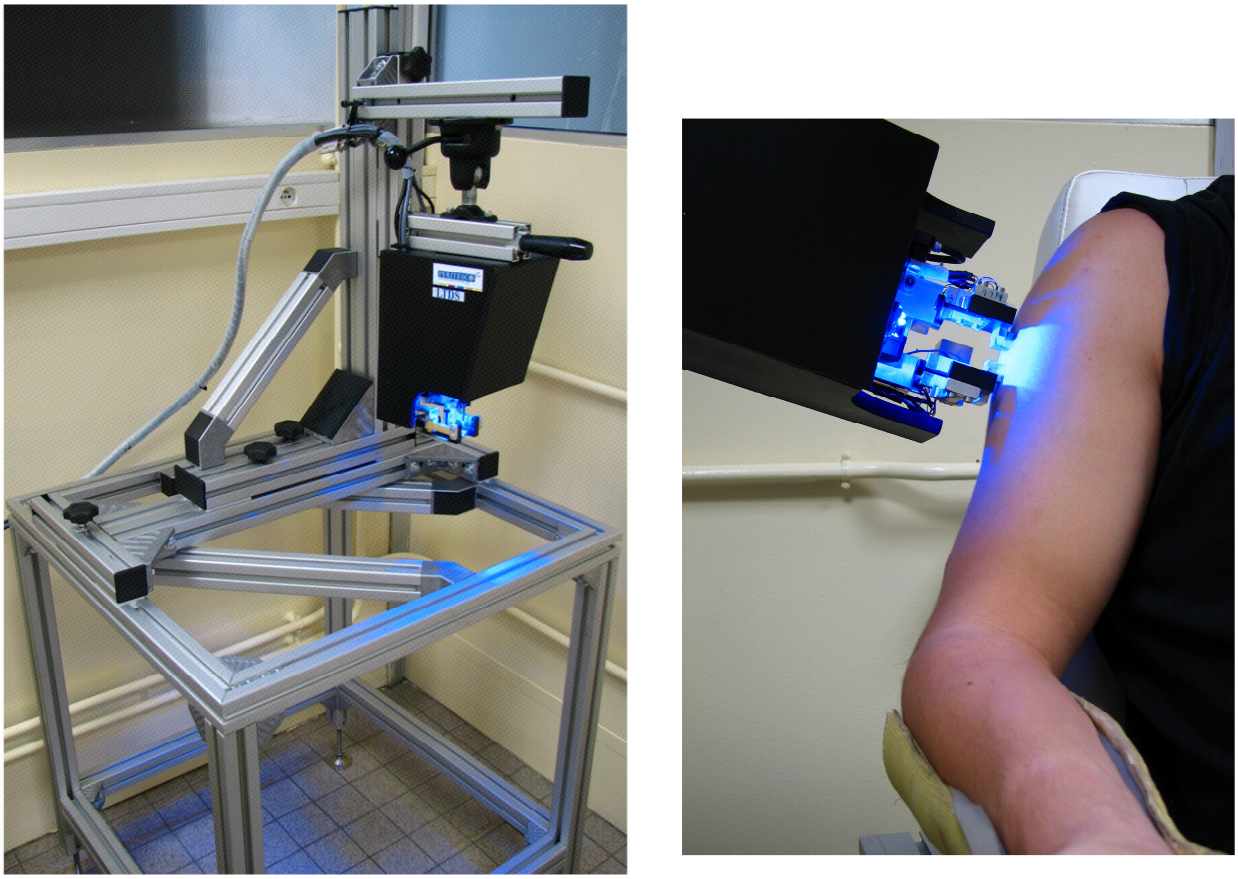

Figure 2. Whole system mounted on a movable frame (left). Measuring head can be rotated to fit with human body necessities, as shown on the right (*in vivo* test on the arm).

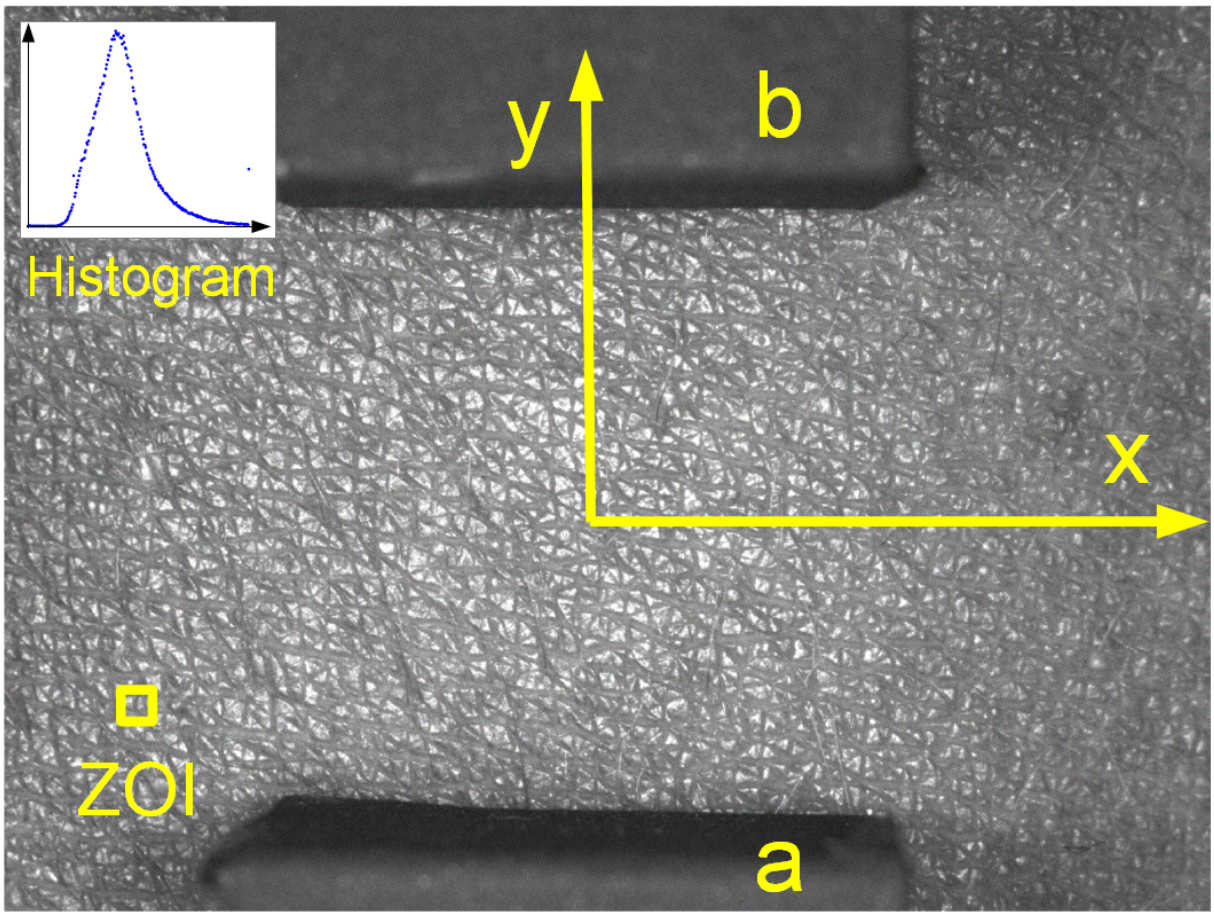

Figure 3. View of the camera: static (a) and movable (b) pads, current frame of reference (x,y). Histogram (full scale: 256 grey levels) and Zone Of Interest (ZOI) have been represented on the upper and lower left angles.

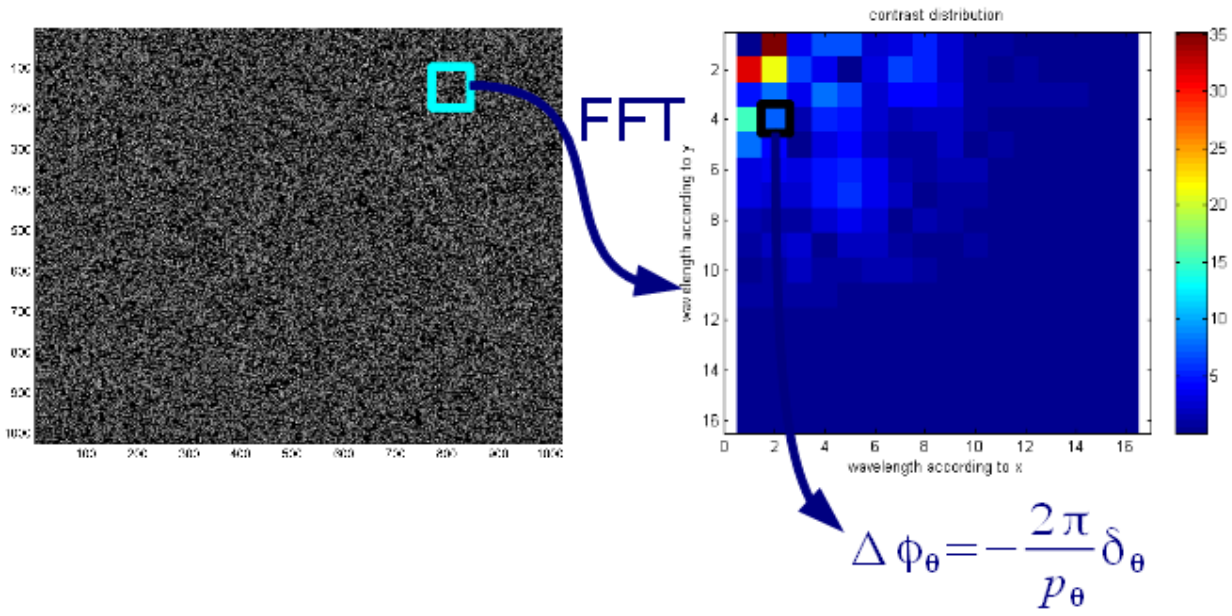

Figure 4. Basic principle of sub-pixel algorithm.

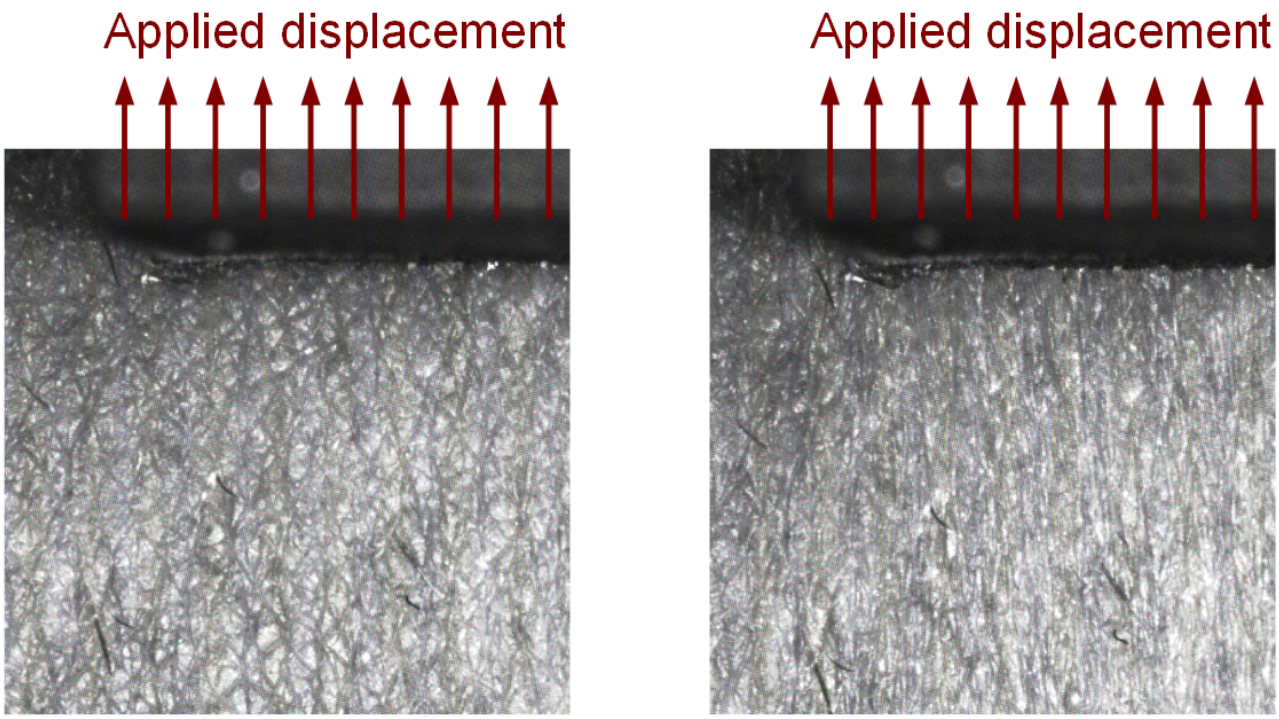

Figure 5. Reference (left) and deformed (right) image of the same area.

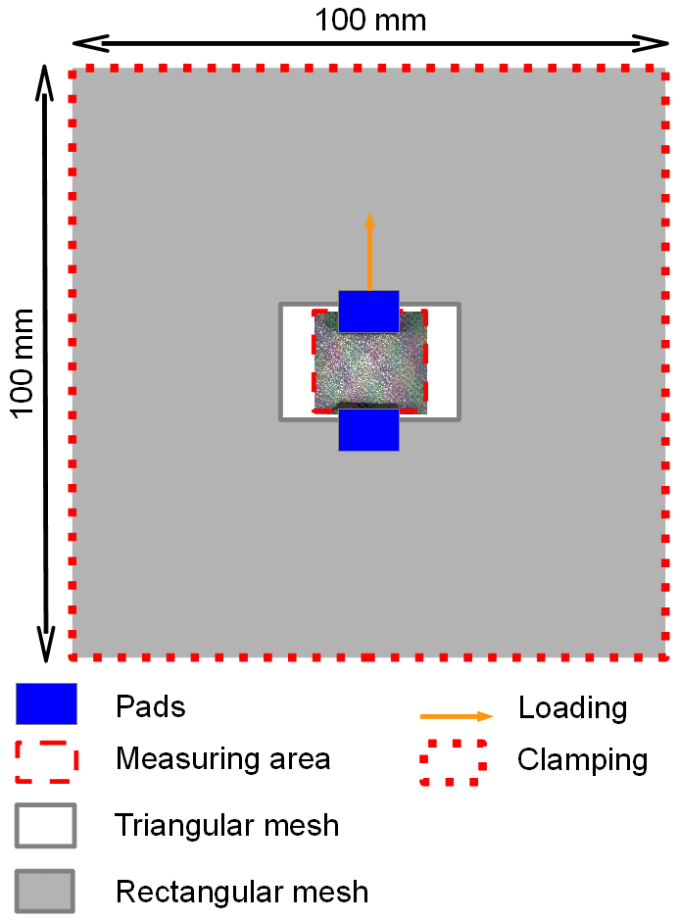

Figure 6. Numerical model.

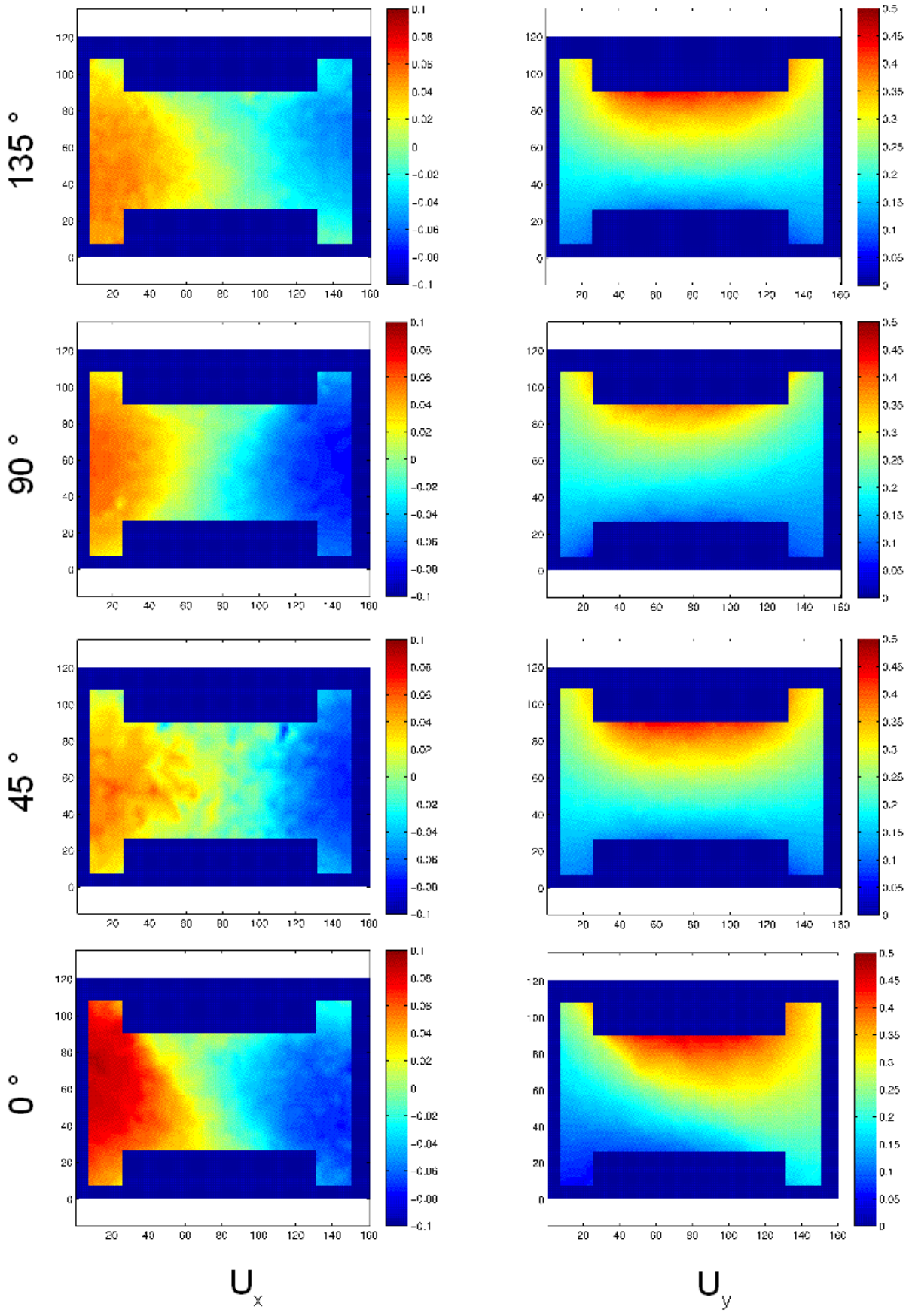

Figure 7. Displacement fields along $\vec{X}$ and $\vec{Y}$ with various tension direction on a woman forearm (young group).

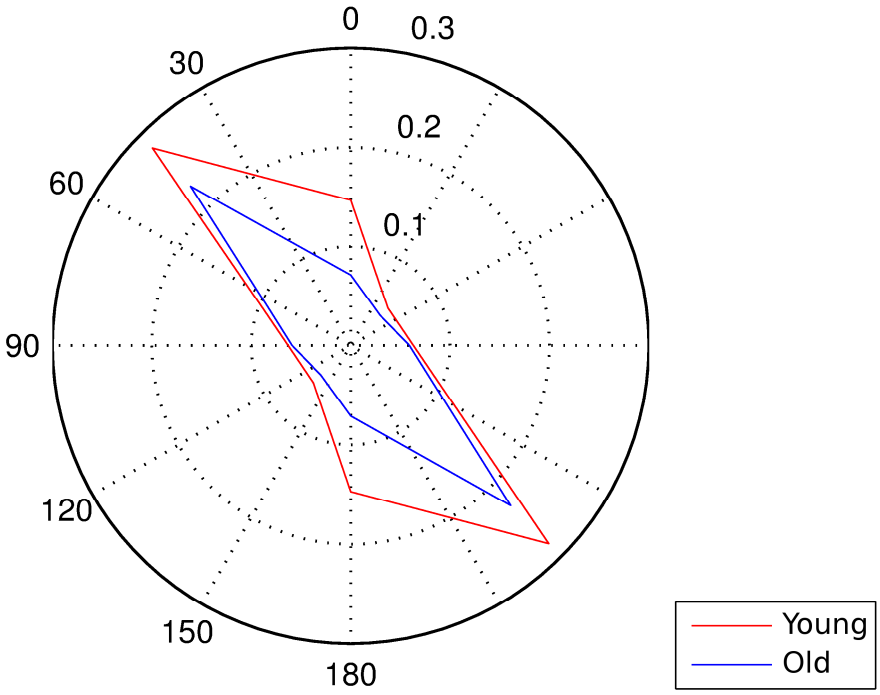

Figure 8. Tangential force F (in N) on static and movable pad (mean values for each group).

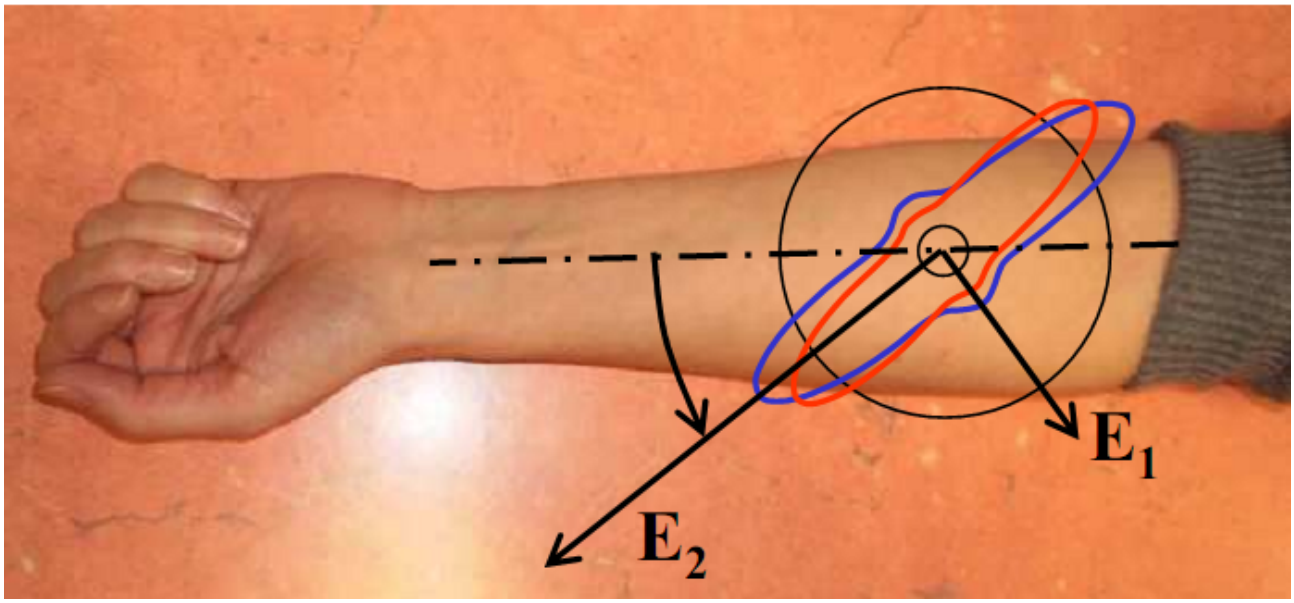

Figure 9. Apparent skin stiffness on the forearm according to the direction.

Figure 10. Forearm positioning apparatus.